A Parametric-Model-Based Approach for Atmospheric Phase Screen Removal in Ground-Based Interferometric SAR

Elisa Giusti , *Member, IEEE*, Samuele Gelli, and Marco Martorella , *Fellow, IEEE*

Abstract—The atmosphere affects the propagation of radar signals by provoking unwanted signal phase changes. In interferometric applications, such as coherent change detection and displacement measurements, this effect may significantly degrade the system performances. Moreover, atmosphere-induced phase changes are both time and space variants, and therefore, they are not easy to be removed. This article proposes a novel method to remove atmospheric effects by using a parametric model of the refractive index, which is derived as an extension of the International Telecommunication Union—Radiocommunication model. The proposed algorithm has been tested on real data acquired by using a ground-based synthetic aperture radar system in conjunction with data collected by a weather station. Data have been acquired continuously for three consecutive days, approximatively every 5 min. Results have shown how the proposed method can effectively remove atmospheric effects and restore the signal phase.

Index Terms—Atmospheric phase screen (APS), ground-based synthetic aperture radar (GB-SAR), SAR interferometry.

I. INTRODUCTION

GROUND-BASED synthetic aperture radar (GB-SAR) interferometry represents a valid tool for the monitoring of small area because of its short revisiting time and its zero spatial baseline [1]–[4] and has been widely used to detect and measure terrain displacement. GB-SAR uses the highly sensitivity of the signal phase to monitor the terrain surface. When terrain displacements occur in a time elapsed between two SAR acquisitions, the phase will vary accordingly. Interferometric SAR (InSAR) exploits this effect for terrain monitoring. The displacement map, i.e., the interferogram, is generally obtained taking the phase of the complex product of two SAR images. Moreover, the use of multiacquisition coherent processing, such as differential InSAR, has boosted the application of SAR in

support of quantitative analysis in many fields of environmental risks, such as volcanic, seismic, and landslide risks.

InSAR data are affected by many factors that cause the presence of spurious phase signals, which act as error sources and impact, if not properly accounted for, the quality of the final deformation results.

Although the zero baseline permits to minimize spatial decorrelation effects when using the GB-SAR system, the interferometric phase may be affected by atmospheric artifacts, typically referred as the atmospheric phase screen (APS). The APS is the most relevant disturbance for GB-SAR measurements, and it might change the true phase signature of the terrain deformation.

Atmospheric delays are, in general, divided into ionospheric and tropospheric terms. Delays in the ionosphere are due to the free electron density. Tropospheric delays are characterized as nondispersive effects resulting from variations in pressure, temperature, and humidity [5].

However, it is the troposphere that has the greatest impact on the interferometric phase in the case of GB-SAR systems, as declared in many papers (see, for example, [4], [6], and [7]).

Many algorithms have been proposed in the literature to address this issue that can be sketchily divided into two main classes, namely, model-based [4], [8]–[10] and data-driven approaches [1]–[3], [11]–[17]. The papers [8] and [10] refer to the satellite system instead of GB-SAR. However, they have been mentioned here as they propose methods using refractive index models that depend on atmospheric parameters, which can then be useful for APS removal regardless of the radar platform.

The first class of algorithms is based on the knowledge of auxiliary data, such as pressure, temperature, and humidity, and of a model of the refractive index to estimate the interferogram degradation due to the atmospheric effects. These methods have the advantage of using a model that preserves the physical consistency of the propagation delay without altering the true terrain displacement. However, weather measurements have the limitation of lower spatial resolution. In addition, they could not be temporally synchronized with the SAR acquisitions and, therefore, need interpolation that may lead to further uncertainties. These methods are, in general, less accurate with respect to the data-driven approaches, and in particular, their accuracy depends on how well the refractive index model matches with the acquired data.

Elisa Giusti and Samuele Gelli are with the Radar and Surveillance System National Laboratory, National Inter-University Consortium for Telecommunications, 56124 Pisa, Italy (e-mail: elisa.giusti@cnit.it; samuele.gelli@cnit.it).

Marco Martorella is with the Department of Information Engineering, University of Pisa, 56122 Pisa, Italy, and also with the Radar and Surveillance System National Laboratory, National Inter-University Consortium for Telecommunications, 56124 Pisa, Italy (e-mail: m.martorella@iet.unipi.it).

The second class of techniques uses the measured interferometric phase and, in some cases, geometrical data of the observed area. These methods model the atmospheric contribution spatially and estimate the model parameters using the measured interferometric phase of some selected persistent scatterers, namely, those scatterers that are supposed to be stationary over time. These methods are not based on any physical model of the refractive index, and their effectiveness is strongly related to the way the persistent scatterers are extracted from the SAR images. These methods generally exhibit good performance, but the estimated atmospheric phase term may be corrupted by nonstationary and tiny terrain deformations. In fact, permanent scatterers are typically selected using their coherence degree. However, movements of the order of a millimeter or even smaller cannot be detected using the coherence degree, which remain high. Therefore, some of the selected permanent scatterers may be actually moving scatterers and may impact on the estimation performance.

This article proposes an approach that can be considered in the middle between the model-based and data-driven approaches. The proposed method partly derived from an extensively analysis on real data acquired in a measurement campaign and partly from the algorithm proposed in [4]. Iannini and Guarnieri [4] proposed a refinement of the refractive model using a humidity calibration step, which leads to significant improvements in the compensation performance. More specifically, the optimization algorithm resorts to find the humidity model's parameters that maximize the average coherence of the selected ground control points (GCPs). The humidity model's parameters have been searched according to a brute force method by computing the average coherence for each parameter set. Although this approach makes use of the measured phase of the GCPs, it is considered as a model-based approach since it still relies on a refractive index model, and as a consequence, it is able to preserve a physical consistency. Following this idea, this article proposes the use of a parametric model of the refractive index, which, nevertheless, preserves the physical value of the model itself. The optimization algorithm in this case is based on a least squares error (LSE) approach applied to the time history of the interferometric phase of spatially distributed persistent scatterers. A closed-form solution can be found for the optimization problem when at least two uncorrelated master–slave pairs are available. A statistical analysis of the APS is carried out using real data, and the proposed algorithm is validated using cooperative scatterers for which the ground truth is available.

The rest of this article is organized as follows. The signal model and the International Telecommunication Union—Radiocommunication (ITU-R) model are presented in Section II. Section III presents a correlation-based analysis conducted onto the measured data that has motivated our work and the algorithm described in Section IV. Section IV presents the results obtained using real data acquired in Italy using a GB-SAR system and cooperative corner reflectors. Discussions on the proposed approach are presented in Section VI. Finally, Section VII concludes this article.

II. SIGNAL MODELING

A. Interferometric Phase

The signal model of a scatterer in the SAR image can be modeled as follows:

$$s_p(i) = a(i)\exp(j\phi_p(i)) + w(i) \tag{1}$$

where i indicates the central time instant at which the SAR image was taken, $a(i)$ represents the overall amplitude signal that may change over time, $\phi_p(i)$ is the scatterer phase over time, and w is the noise component.

The scatterer phase can be written as follows:

$$\phi_p(i) = \phi_{0,p} + \frac{4\pi}{\lambda} \int_{L_p} n(\mathbf{r}, i) d\mathbf{r} \tag{2}$$

where $\phi_{0,p}$ is the scatterer radar cross section phase, L_p is the path that the wavelength travels to reach the scatterer and come back to the radar, and $n(\mathbf{r}, i)$ is the refractive index that may change spatially and temporally defined as follows:

$$n(\mathbf{r}, i) = \frac{c}{v(\mathbf{r}, i)} = 1 + 10^{-6} N(\mathbf{r}, i) \tag{3}$$

where c is the speed of light in a vacuum, $v(\mathbf{r}, i)$ is the light speed in the medium, and $N(\mathbf{r}, i)$ is a function that depends on the meteorological parameters over time.

In many applications, it is commonly assumed that the refractive index is spatially homogeneous and that only varies over time. This is especially true for GB-SAR applications, where the observed area is small and the radar has a limited altitude with respect to the area to observe. Under this hypothesis, (2) can be approximated as follows:

$$\phi_p(i) = \phi_{0,p} + \frac{4\pi}{\lambda} r_p n(i) \tag{4}$$

where r_p is the line-of-sight (LoS) distance of the scatterer to the radar. The interferometric phase is computed as the difference between the scatterer's phase values at different times, as follows:

$$\Delta\phi_p(k) = \phi_{0,p} + \frac{4\pi}{\lambda} r_p \Delta N(k) \tag{5}$$

where k is the time lag between reference and secondary images and $\Delta N(k)$ relates with the refractive index variation over time and depends on temperature, pressure, and humidity changes. As it can be noted, the refractive index changes affect the correct estimation of the scatterer's phase term, namely, $\phi_{0,p}$, which contains the information related to the scatterer's movement occurred in the time interval between reference and secondary acquisitions. To reach precise estimation of scatterer movement, the phase component due to the refractive index changes needs to be removed or at least mitigated.

B. Refractivity Index Model

The refractive index is determined by both the ionosphere and the troposphere. However, as mentioned in many other papers, the ionospheric contribution can be neglected in GB-SAR applications [4], [6], [7]. According to the ITU-R standards [18],

the refractive index can be modeled as composed of two main components, as follows:

$$N(i) = N_{\text{dry}}(i) + N_{\text{wet}}(i)$$
$$= 0.2589 \frac{P_d(i)}{T(i)} + \left(71.7 + \frac{3.744}{T(i)10^5} \right) \frac{e(i)}{T(i)}. \quad (6)$$

The dry component $N_{\text{dry}}(i)$ is related to the temperature $T(i)$ and the spatial pressure of the dry gasses $P_d(i)$, while the wet component N_{wet} is related to the partial pressure of the water vapor $e(i)$ and the temperature. P_d is expressed in millibar and T is expressed in Kelvins. The water pressure can be computed by using the Magnus–Teten formula [6], as follows:

$$e(i) = \frac{h(i)E(i)}{100} \quad (7)$$

where

$$E(i) = 6.10781 \cdot \exp \left\{ \frac{17.2693 \, (T(i) - 273.16)}{T(i) - 35.86} \right\} \quad (8)$$

and $h(i)$ is the humidity expressed in percentage.

As specified in [18], the expression in (6) can be used for all radio frequencies.

III. CORRELATION-BASED ANALYSIS OF THE REFRACTIVE INDEX MODEL

To understand how well the refractive index defined in (8) fits with the acquired data, the correlation between the measured refractive index variation and ΔN_{dry}, ΔN_{wet}, and ΔN, calculated using (8), has been analyzed considering different temporal batches and three scatterers. The time of the reference image is "23-Sep-19:50." The secondary images have been acquired every 5 min for roughly 22 h (till "24-Sep-18:00"). We have considered time batches of roughly 4 h each. In each time interval, the correlation has been calculated, and some of the results are shown in Fig. 1.

The degree of correlation can be evaluated by observing the maximum value of the cross correlation. As can be observed, it does not always assume high values, as, for example, in the fourth and fifth time intervals. Moreover, the peaks in some cases are at time instants different from the central one, meaning that a certain degree of correlation exists but with a time-shifted version of the refractive index, which is, however, unexpected. It is worth noting that the behavior of the dry and wet components changes over time and behaves differently. As, for example, in the second and third time intervals, the dry component exhibits a high and negative correlation with the measured refractive index variation. Conversely, the wet component exhibits a low and positive correlation value. The opposite can be observed instead in the second-last time interval, where the wet component has a negative and high correlation value, while the dry component has a low correlation value. This analysis has been conducted for many other data frames, and similar results have been observed. In general, it can be observed that a low correlation value of ΔN_{dry} and/or ΔN_{wet} affects the correlation between the measured refractive index variation and the

ITU-R refractive index model, as shown in the third column of Fig. 1. In fact, the ITU-R model equally balances the wet and dry components. This analysis shows that the ITU-R model not always well matches with the measured data and suggests that the dry and wet components should be better combined to reach the highest correlation value according to an optimization criterion.

IV. PROPOSED APPROACH

The refractive index model defined in the previous sections depends on the number of atmospheric parameters that should be measured close to the measurement site and, at the same time, on the number of the radar measures. However, weather stations cannot be always available in the area of interest, especially when the area to monitor is not easily accessible or when implementing repeat pass interferometry using an airborne radar system. By taking this in mind, an approach that can be considered in the middle between the model-based and data-driven approaches is proposed in this section. The proposed method has been inspired partly from the correlation-based analysis presented in Section III and partly from what proposed in [4]. Particularly, Iannini and Guarnieri [4] proposed a refinement of the refractive index model by modeling the humidity as a first-order polynomial $h(\alpha, \beta; i) = \alpha h(i) + \beta$. Then, the optimization algorithms estimate (α, β) that maximize the average coherence of the selected GCPs. The optimization is carried out using a brute force method by computing the average coherence for each (α, β) pair.

Although this approach makes use of the measured phase of the GCPs, it is considered as a model-based approach since it still relies on the refractive index model, and as a consequence, it is able to preserve a physical consistency. The authors, however, do not provide any justification about the choice of that particular model for the humidity.

Following this idea, a parametric model-based approach is defined as

$$\Delta N = \alpha \Delta N_{\text{dry}} + \beta \Delta N_{\text{wet}} \quad (9)$$

where ΔN, ΔN_{dry}, and ΔN_{wet} are the refractive index variation, the dry component variation, and the wet component variation over time, respectively, and α and β are the two parameters to estimate. Equation (9) clearly states that the refractive index is a linear combination of ΔN_{dry} and ΔN_{wet}.

The proposed algorithm goal is to choose α and β that minimize the mean square error of the residual interferometric phase after APS removal of the GCPs. The optimization criteria can be mathematically defined as follows:

$$(\alpha_s, \beta_s)$$
$$= \operatorname*{argmin}_{\alpha, \beta} \left\{ \sum_{n_t} \left(\Delta \phi(n_t) - \frac{4\pi f}{c} r \Delta N(\alpha, \beta; n_t) \right)^2 \right\} \quad (10)$$

where n_t is the time difference between a reference–secondary pair and r is the range of a scatterer. Obviously, (10) relies on the assumption that the measured phase refers to a stationary
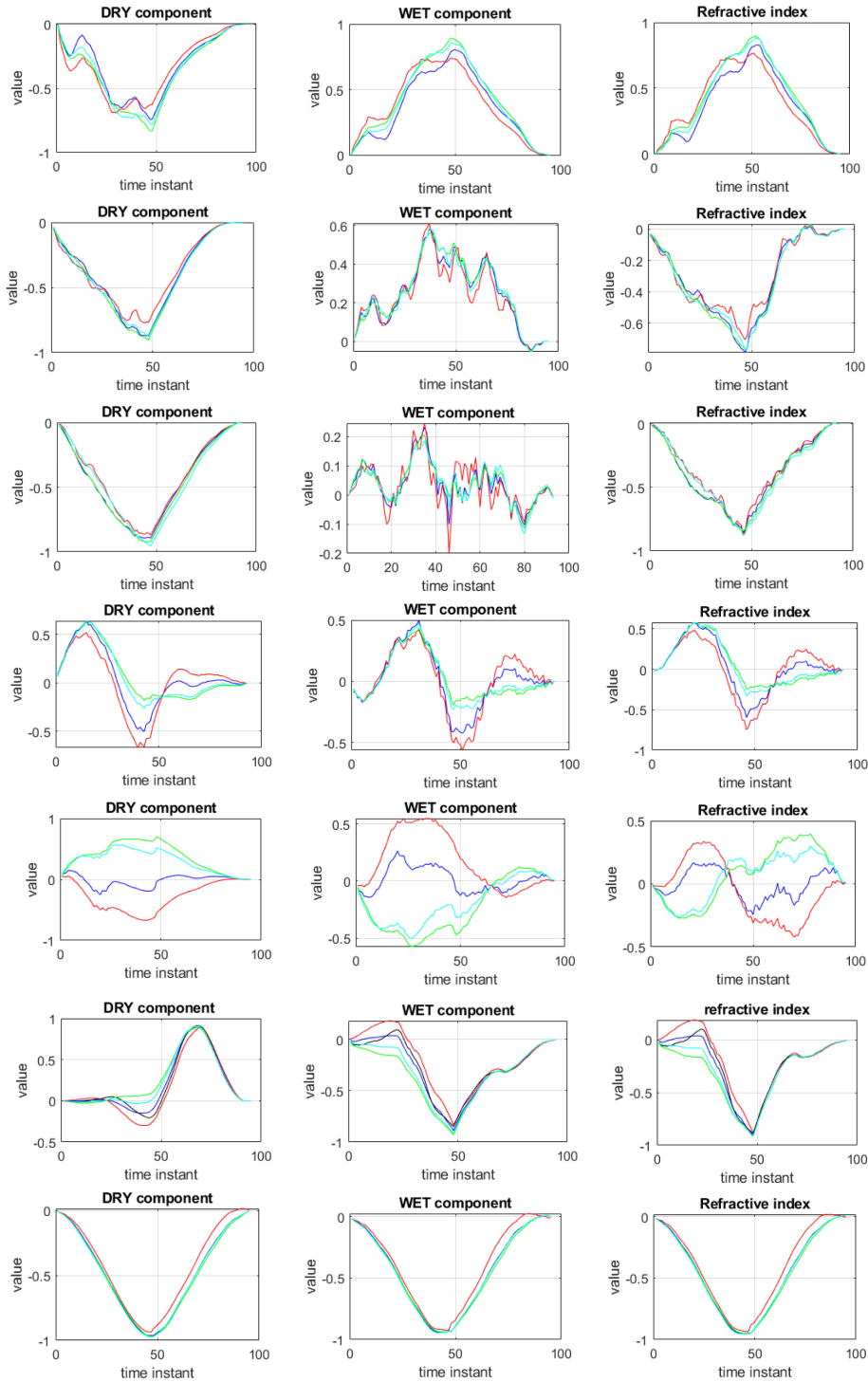
Fig. 1. Cross-correlation results. Each row refers to a different time interval. The images in the first, second, and third columns are the cross correlations between the measured refractive index variation, measured from the interferometric phase, and ΔN_{dry}, ΔN_{wet}, and ΔN, as calculated in (8), respectively. Colors refer to four cooperative corner reflectors, those with the highest coherence.

scatterer, namely, a scatterer whose interferometric phase is expected to be zero in absence of phase artifacts due to the atmosphere. To mitigate the spatial variability of the refractive index, several spatially distributed GCPs can be considered, and the optimization problem in (10) applied to each one. The α and β parameters are, then, computed as the mean values of the estimated ones, as follows:

$$\hat{\alpha} = \frac{1}{N_S} \sum_s \alpha_s$$

$$\hat{\beta} = \frac{1}{N_S} \sum_s \beta_s \qquad (11)$$

where N_S is the number of GCPs, s is the GCP index, and α_S and β_S are estimated using (10) for each scatterer separately. It is possible to demonstrate that a closed-form solution of (10) exists when at least two reference–secondary pairs are available.

The LSE closed-form solution can be found by equating the derivatives of the squared error to zero, i.e.,

$$\frac{\delta\epsilon}{\delta\alpha} = 0$$
$$\frac{\delta\epsilon}{\delta\beta} = 0 \tag{12}$$

where $\epsilon = \sum_{n_t} (\Delta\phi(n_t) - \frac{4\pi f}{c} r \Delta N(\alpha, \beta; n_t))^2$.

By calculating the derivative of ϵ with respect to the parameters α and β and equating them to zero, the following solutions can be found:

$$\beta = \frac{\sum_{n_t} \Delta\phi(n_t) \cdot \Delta\phi_{W,n_t} - A}{\sum_{n_t} \Delta\phi^2_{W,n_t} - B}$$

$$\alpha = \frac{\sum_{n_t} \Delta\phi_{n_t} \Delta\phi_{D,n_t}}{\sum_{n_t} \Delta\phi^2_{D,n_t}} - \beta \cdot \frac{\sum_{n_t} \Delta\phi_{W,n_t} \Delta\phi_{D,n_t}}{\sum_{n_t} \Delta\phi^2_{D,n_t}} \tag{13}$$

where $\Delta\phi_{W,n_t} = \frac{4\pi f}{c} r \Delta N_{\text{wet}}$ and $\Delta\phi_{D,n_t} = \frac{4\pi f}{c} r \Delta N_{\text{dry}}$ are the phase changes due to the wet and dry components, respectively, and

$$A = \frac{\sum_{n_t} \Delta\phi_{D,n_t} \Delta\phi_{W,n_t} \cdot \sum_{n_t} \Delta\phi_{n_t} \Delta\phi_{D,n_t}}{\sum_{n_t} \Delta\phi^2_{D,n_t}} \tag{14}$$

$$B = \frac{\sum_{n_t} \Delta\phi_{D,n_t} \Delta\phi_{W,n_t} \cdot \sum_{n_t} \Delta\phi_{W,n_t} \Delta\phi_{D,n_t}}{\sum_{n_t} \Delta\phi^2_{D,n_t}}. \tag{15}$$

Particularly, as it will be better clarified later on in this article, $(\hat{\alpha}, \hat{\beta})$ are calculated in each time batch but always using the same reference SAR image. In other words, the reference image is kept fixed, while a number of secondary images are considered in the selected time batch. This estimate is repeated in each time batch. The time batches partly overlap to ensure continuity. Time batches of 4 h are used in this document. Different time batch lengths have been tested, but the differences were negligible. From our analysis, a time interval of 4 h was sufficient to handle the diurnal cycle, i.e., the variations in meteorological parameters during the day.

V. MEASUREMENT CAMPAIGN

A measurement campaigns have been conducted using a GB-SAR system developed by ECHOES s.r.l. company. A picture of the PHOENIX GB-SAR system is shown in Fig. 2. The radar transmits a frequency-modulated continuous-wave (FMCW) waveform.

The radar system can be tilted from $-40°$ to $60°$ with respect to the horizon with an angular step of $5°$. The radar can be remotely controlled connecting it to a remote desktop via a Gbit Ethernet. The radar main technical specifications are summarized in Table I.

(a)

(b)

Fig. 2. (a) and (b) Pictures of the PHOENIX GB-SAR system and its rail.

TABLE I
RADAR SPECIFICATIONS

Along track speed	Up to $20cm/s$
Waveform type	FMCW
Sampling rate	$5MS/s$
Transmitted peak power	$16dBm$
Range resolution	$0.15m$
Antenna gain	$15dB$
Angular resolution	$0.4°$
Antenna elevation aperture	$31°$
Cross range resolution	$8m@1000m$
Operating voltage	$18 - 28VDC$
Angular coverage	$520m@1000m$
Power consumption	$50 - 70W$
Polarization	Linear H

A. Dataset and Measurements Sites Description

The Poggio Baldi landslide, located near Corniolo in the municipality of Santa Sofia, Italy, is a landslide, where in 2010 a massive rock fall occurred. This is considered as a reactivation of a landslide, occurred in 1914. In this area, since 2015, an Experimental Landslide Monitoring Site has been developed for research purposes using different systems of measurements, where monitoring instrument can be tested and calibrated. The measurement site is shown in Fig. 3. The area is composed of two areas with different inclination: the highest part is landslide deposits and the lowest part is not in evolution. The latter, in particular, was used for our measurements.

During experiments, cooperative targets have been placed in the selected scene and used as benchmark with the aim of estimating the subsidence accuracy. In particular, five corner reflectors have been placed, as shown in Fig. 4. More specifically,
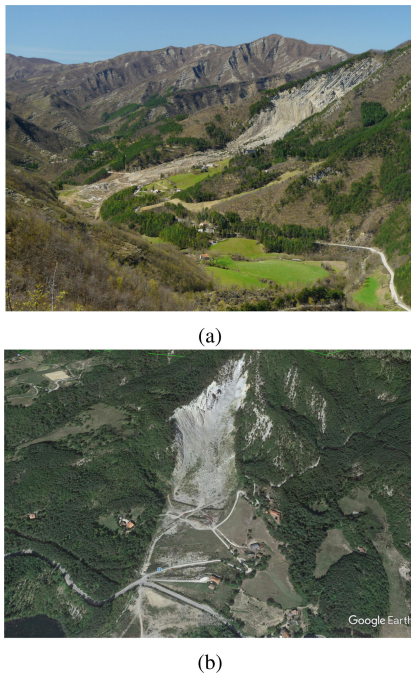
(a)

(b)

Fig. 3.   (a) Lateral and (b) satellite views of Poggio Baldi Landslide.
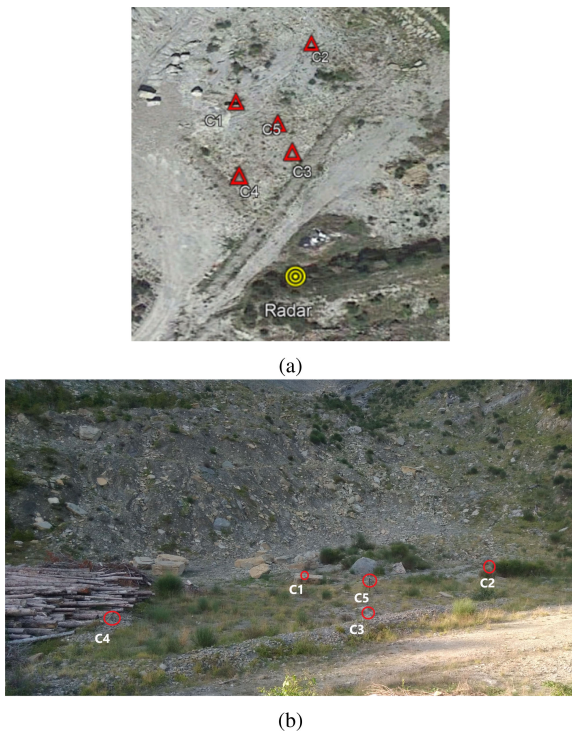

(a)

(b)

Fig. 4.   (a) Measurement configuration of corner reflectors and radar. (b) Corner configuration from the radar position.

the picture in Fig. 4(b) shows the corner disposition as seen by the radar.

Corner #5 has been placed on a submillimeter graded tripod, while the others have been placed onto the ground or fixed on rocks using bolts. Auxiliary systems were also used to monitor the weather parameters over time during the whole measurement

time, and more specifically, an optical camera, a professional thermal camera, and a weather station were used to measure temperature, pressure, wind and rain, and two humidity sensors.

B. Results

Before illustrating the results, it is convenient to describe the performance indexes that have been used to numerically evaluate the proposed approach. Results will be provided in terms of the interferometric phase plots before and after the atmospheric phase compensation algorithms. Both the proposed one and the standard ITU-R model have been used for the purpose of comparison. The histogram of the residual phase term after compensation has also been considered in order to visual understand how well the compensation algorithms remove the atmospheric artifacts. Based on the histogram, the mean value and the standard deviation of the residual phase are also evaluated both in radians and in meters. The residual phase term can be easily evaluated as follows:

$$\Delta\phi_{\mathrm{res}} = \Delta\phi(n_t) - \frac{4\pi f}{c}r\Delta N_i \qquad (16)$$

where $i = 1, 2$ and ΔN_1 is the refractive index variation estimated using the ITU-R model, while ΔN_2 is the refractive index variation estimated using the proposed model. Finally, the measured refractive index variation has been compared with the estimated ones in a plot, in order to visually evaluate how well the estimated refractive index variation matches with the measured one. The measured refractive index variation can be computed as follows:

$$\Delta N_m(n_t) = \frac{\Delta\phi c}{4\pi f r}. \qquad (17)$$

The analysis that follows has been conducted by selecting a certain number of corner reflectors. The atmospheric phase compensation algorithms have been applied to two datasets corresponding to approximately 15 h each. The proposed algorithm has been applied using a moving window approach, as already explained in Section III. Particularly, the model parameters, namely, $(\hat{\alpha}, \hat{\beta})$, have been estimated using a 4-h time window sliding over the dataset. This approach gives an estimate of $(\hat{\alpha}, \hat{\beta})$ at every time batch. Fig. 5 shows the estimates at each considered scatterer. As can be observed, 15 estimates are obtained because time batches of 3 h each overlap. It is worth remarking that the reference image is kept fixed, and it is the same for all the secondary images of all time batches. The thin colored lines correspond to the different GCPs, while the thick blue line represents the mean values, namely, $(\hat{\alpha}, \hat{\beta})$, which are used for compensating the interferometric phase.

As can be observed, the same trend can be observed for all the scatterers even though some differences exist in their values.

Four of the five corner reflectors have been used as PSs. In fact, by observing the scatterer coherence in a time lap of about one day shown in Fig. 6, it can be observed that scatterer #3 exhibits a low coherence value with respect to the others.

Fig. 7 shows the results of the atmospheric compensation algorithms. In particular, the colored dashed lines represent the interferometric phase of each scatterer before the atmospheric
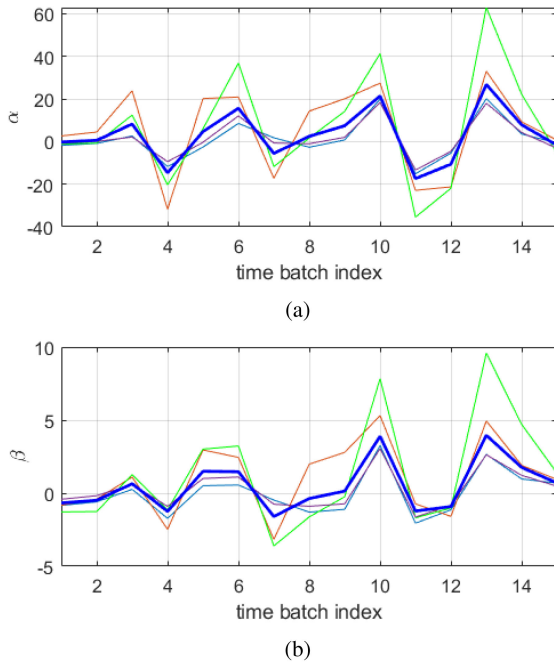
Fig. 5. (a) and (b) Estimates of (α, β) over time, namely, over different time batches. Thin colored lines relate to the different scatterers, while the thick blue line represents the mean values of the estimates, namely, $(\hat{\alpha}, \hat{\beta})$.

TABLE II
MEAN VALUE AND STANDARD DEVIATION OF THE HISTOGRAMS IN FIG. 8, IN RADIANS AND IN METERS

	Measured	ITU-R	Proposed
$\mu[rad]$	0.062	0.0631	0.0123
$\sigma[rad]$	0.0485	0.0734	0.0367
$\mu[mm]$	$1.08e-1$	$1.107e-1$	$2.156e-2$
$\sigma[mm]$	$8.52e-2$	$1.28e-1$	$6.433e-2$

phase compensation, and the solid colored lines represent the interferometric phase after the atmospheric phase compensation. The top figure shows the results obtained using the proposed method, while the bottom figure shows the results obtained by using the ITU-R model. The plots refer to the data acquired from 23 September 19:25 to 24 September 12:33.

Fig. 8 shows the histogram of both the measured interferometric phase and the residual interferometric phase after applying the ITU-R and proposed models.

Table II lists the mean value, μ, and the standard deviation, σ, of the residual interferometric phase to numerically quantify the residual error. As can be noted, the proposed method permits to reduce both the mean value (which should be zero) and the standard deviation of the interferometric phase.

Fig. 9 shows the comparison between the estimated refractive index variations for each master–slave pair and the measured one. x and y are, respectively, ΔN_{dry} and ΔN_{wet} computed using (6) and the measured temperature, pressure, and humidity over time. More specifically, the green dots are the measured refractive index variation computed for each master–slave

pair and for each scatterer using (17). The red dots represent the refractive index variation computed according to the ITU-R model. The blue dots represent the refractive index variation computed by the proposed approach. As can be observed, the proposed model better fits with the measured values, and this results in a better compensation of the atmospheric effects.

During the second day of acquisition, the corner reflector $C5$ was moved two times: 2 mm at 12:00 and 5 mm at 15:30 of the same day. The displacement was along the radar LoS, so that the scatterer displacement corresponds to a range movement of the same quantity.

This portion of data has been processed as done previously in order to understand if the proposed approach affects the corner displacement estimation.

Fig. 10 shows the interferometric phase before and after the atmospheric phase term removal. The top image refers to the proposed algorithm, while the bottom image refers to the ITU-R model. In both images, the colored dashed lines represent the measured interferometric phase, while the solid colored lines represent the residual interferometric phase after the atmospheric effect mitigation. It is worth noting that the green lines refer to the scatterer that was moved of 2 mm at 12:00 and of 5 mm at 15:30 of the same day. The other scatterers were stationary, and in fact, their interferometric phase remained quite close to zero. The stationary scatterers have been used during the estimation process. Then, the estimated phase has been removed from all the scatterers, including the scatterer $C5$.

To better appreciate the APS compensation onto stationary scatterers, Fig. 11 illustrates a magnification of Fig. 10 in the time interval, in which all the scatterers were stationary. As can be observed, the proposed algorithm slightly outperforms the ITU-R-based algorithm.

A visual inspection of Fig. 10 over the nonstationary scatterer seems to confirm that both the ITU-R-based algorithm and the proposed approach do not greatly affect the interferometric phase of the nonstationary scatterer. However, to better evaluate the effect of the proposed approach onto the interferometric phase of the nonstationary scatterer, Fig. 12 compares the residual interferometric phase with the measured one. More specifically, the dark, green, and pink lines are, respectively, the measured interferometric phase, the interferometric phase after the application of the proposed approach, and the residual interferometric phase after the application of the ITU-R model.

Tables III and IV show the mean value μ, standard deviation σ, and minimum and maximum values of the interferometric phases $\Delta\phi_{min}$ and $\Delta\phi_{max}$, computed in the two time intervals indicated by the markers in Fig. 12. The first time interval is from 12:25 to 14:10, and the second time interval is from 15:40 to 17:40.

The numerical values in Tables III and IV confirm that the measured interferometric phase is only slightly affected by the atmospheric effects. In fact, the mean values computed using the measured interferometric phase are 2.22 and 4.83 mm in the two time intervals, respectively. However, the standard deviation is quite high. This can also be noted by observing $\Delta\phi_{min}$ and
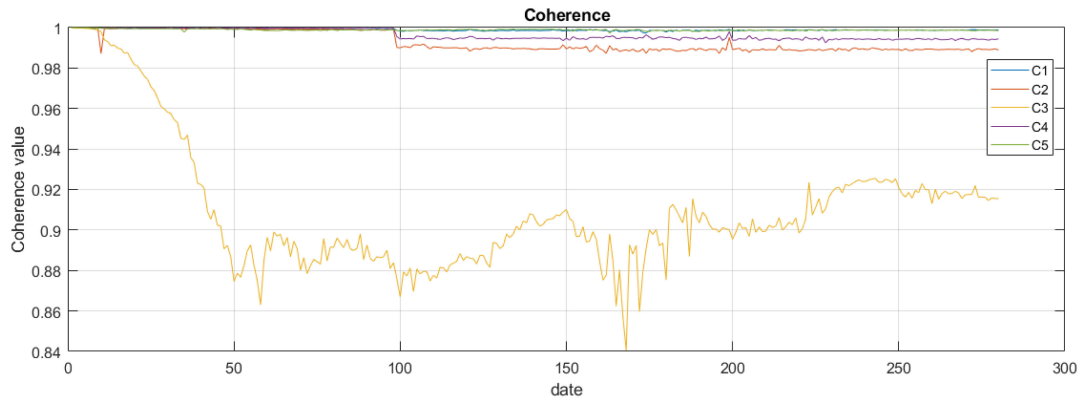
Fig. 6. Coherence of the corner reflector over time in a time laps of about one day.
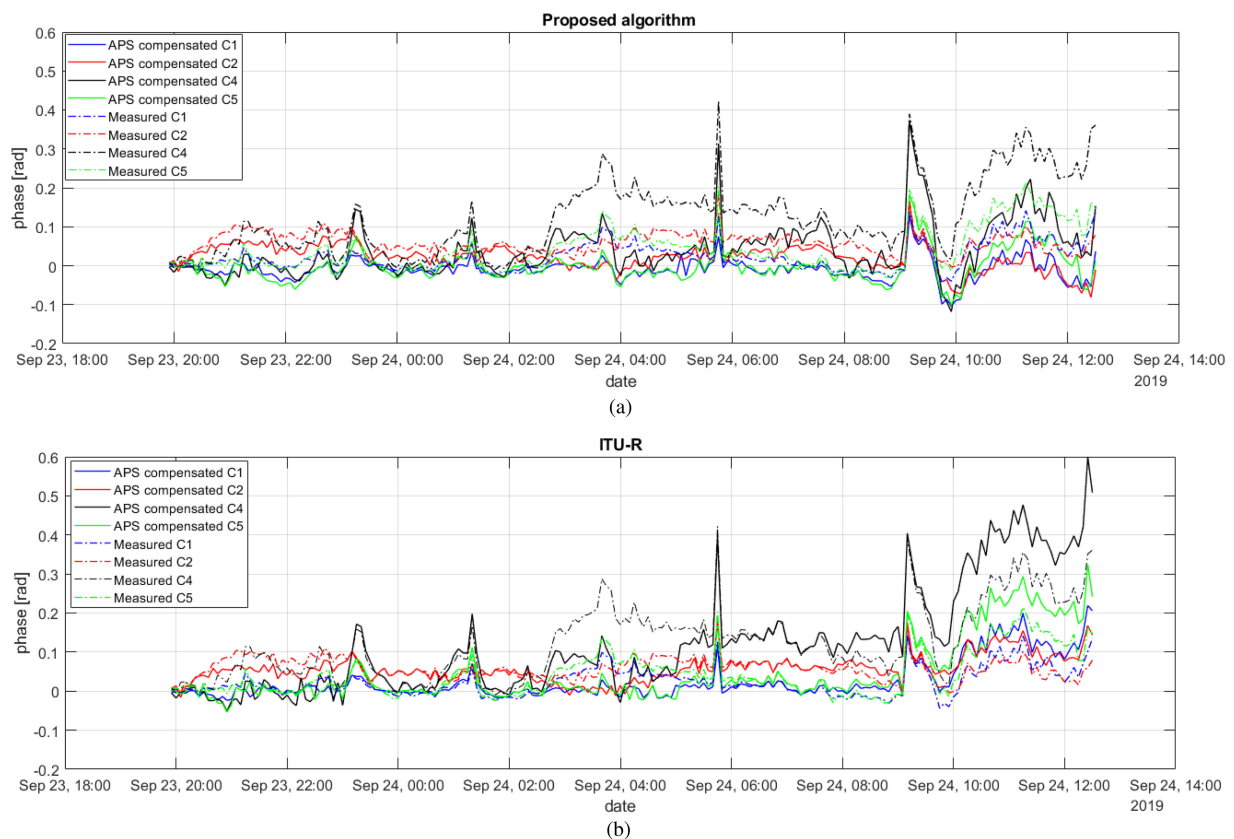

(a)

(b)

Fig. 7. Interferometric phase after atmospheric effect compensation. The top (a) and bottom (b) images refer, respectively, to the application of the proposed approach and of the ITU-R model. In each image, the colored dashed lines represent the measured interferometric phase. Each color refers to a corner reflector. The colored solid lines represent the interferometric phase after the APS compensation. This image refers to data acquired from September 23, 2019 at 19:25 to September 24, 2019 at 12:33.

$\Delta\phi_{\max}$. The proposed approach contributes to reducing the standard deviation of the residual interferometric phase significantly, without drastically affecting its mean value. In fact, the mean values of the residual interferometric phases remain quite close to the true value; more specifically, they are 2.12 and 5.16 mm, respectively, but the standard deviation is reduced. In fact, the residual interferometric phase after the application of the proposed model varies from 1.94 to 2.22 mm and from 4.94 to 5.51 mm for the first and second time intervals, respectively.

Conversely, the application of the ITU-R model while reducing the standard deviation seems to slightly alter the mean value providing a worse estimate of the scatterer movement.

The results in Tables III and IV have been obtained using the scatterers with a coherence greater than 0.9 for the estimate of the refractive index model's parameters. To better evaluate the algorithm stability against the choice of the selected scatterers, a leave-one-out cross validation has been carried out. In other words, the proposed approach has been applied leaving out one

(a)

(b)

Fig. 9. Comparison between the measured and estimated refractive index variations. The 3-D images plot the measured and estimated ΔN using ΔN_{dry} and ΔN_{wet} calculated using (17). Green dots represent the measured ΔN, and red and blue dots correspond to the estimated ΔN using the ITU-R and proposed models, respectively. The images in (b) are top and side views of (a).
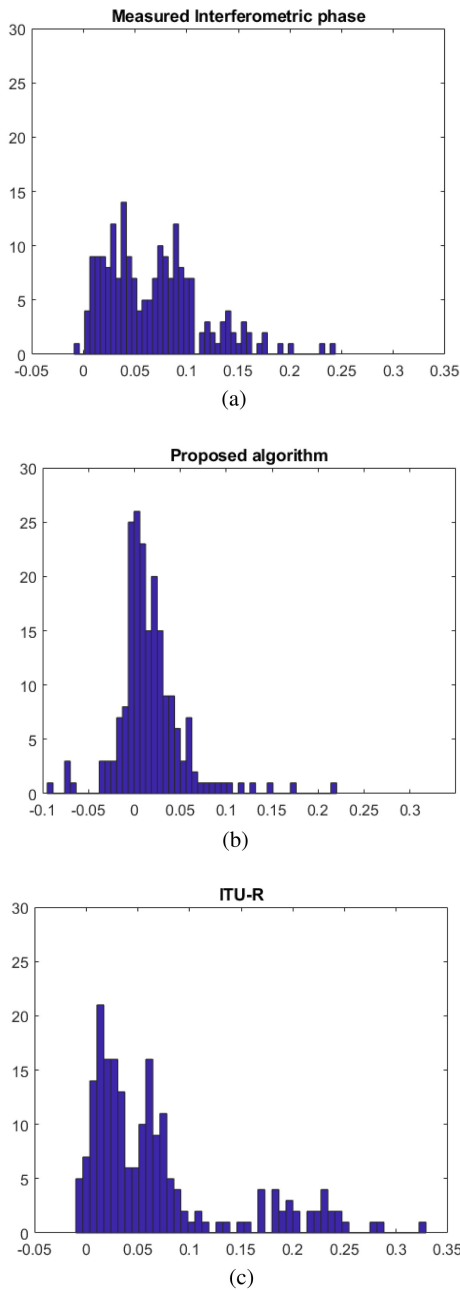

Fig. 8. (a)–(c) Histograms of the interferometric phases before and after atmospheric effect compensation. More specifically, images from top to bottom represent the histograms of the measured interferometric phase, the histograms of the interferometric phase after the application of the proposed approach, and the histograms of the interferometric phase after the application of the ITU-R model.

of the scatterers from the estimation process. Results are shown in Tables V and VI. As can be noted, results similar to those presented above are obtained. The proposed approach always provides good estimates, even better than those in Tables III and IV, especially in the "Leave-$C1$" and "Leave-$C2$" cases. The third experiment, shown in the third column, provides instead slightly worse results but still better than those obtained using the ITU-R model.
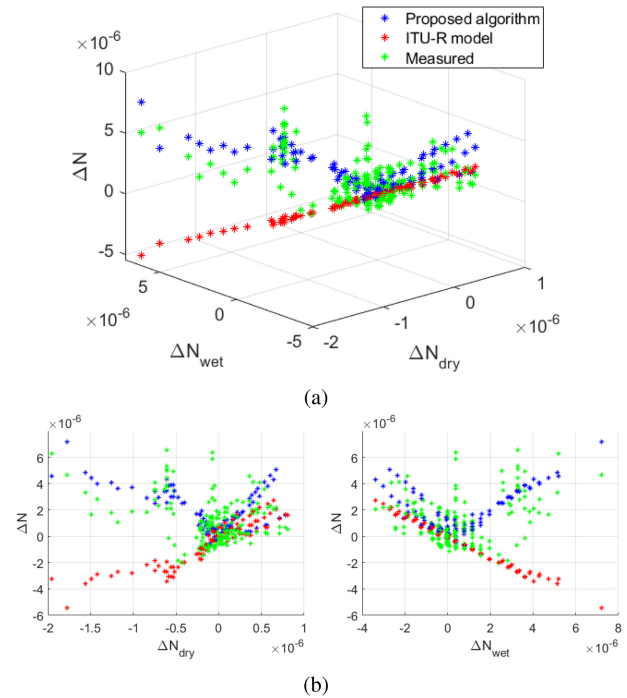
TABLE III
MEASURED STATISTICS OF THE INTERFEROMETRIC PHASE BEFORE AND AFTER ATMOSPHERIC EFFECT MITIGATION

	Measured	ITU-R	Proposed
$\mu[rad]$	1.258669	1.349564	1.212191
$\sigma[rad]$	0.052726	0.030651	0.0314348
$\mu[mm]$	2.209	2.369	2.1278
$\sigma[mm]$	0.092555	0.053804	0.055180
$\Delta\phi_{min}[rad]$	1.076139	1.242588	1.104537
$\Delta\phi_{max}[rad]$	1.348837	1.403237	1.267366
$\Delta\phi_{min}[mm]$	1.889	2.181	1.939
$\Delta\phi_{max}[mm]$	2.368	2.463	2.224

Values refer to the first time interval, when the scatterer is moved of 2 mm.

TABLE IV
MEASURED STATISTICS OF THE INTERFEROMETRIC PHASE BEFORE AND AFTER ATMOSPHERIC EFFECT MITIGATION

	Measured	ITU-R	Proposed
$\mu[rad]$	2.75518	3.05295	2.9424
$\sigma[rad]$	0.18572	0.13063	0.09872
$\mu[mm]$	4.836	5.359	5.165
$\sigma[mm]$	0.326013	0.22929	0.17328
$\Delta\phi_{min}[rad]$	2.55808	2.90301	2.81594
$\Delta\phi_{max}[rad]$	3.16932	3.29086	3.14244
$\Delta\phi_{min}[mm]$	4.490	5.095	4.943
$\Delta\phi_{max}[mm]$	5.563	5.777	5.516

Values refer to the second time interval, when the scatterer is moved of 5 mm.
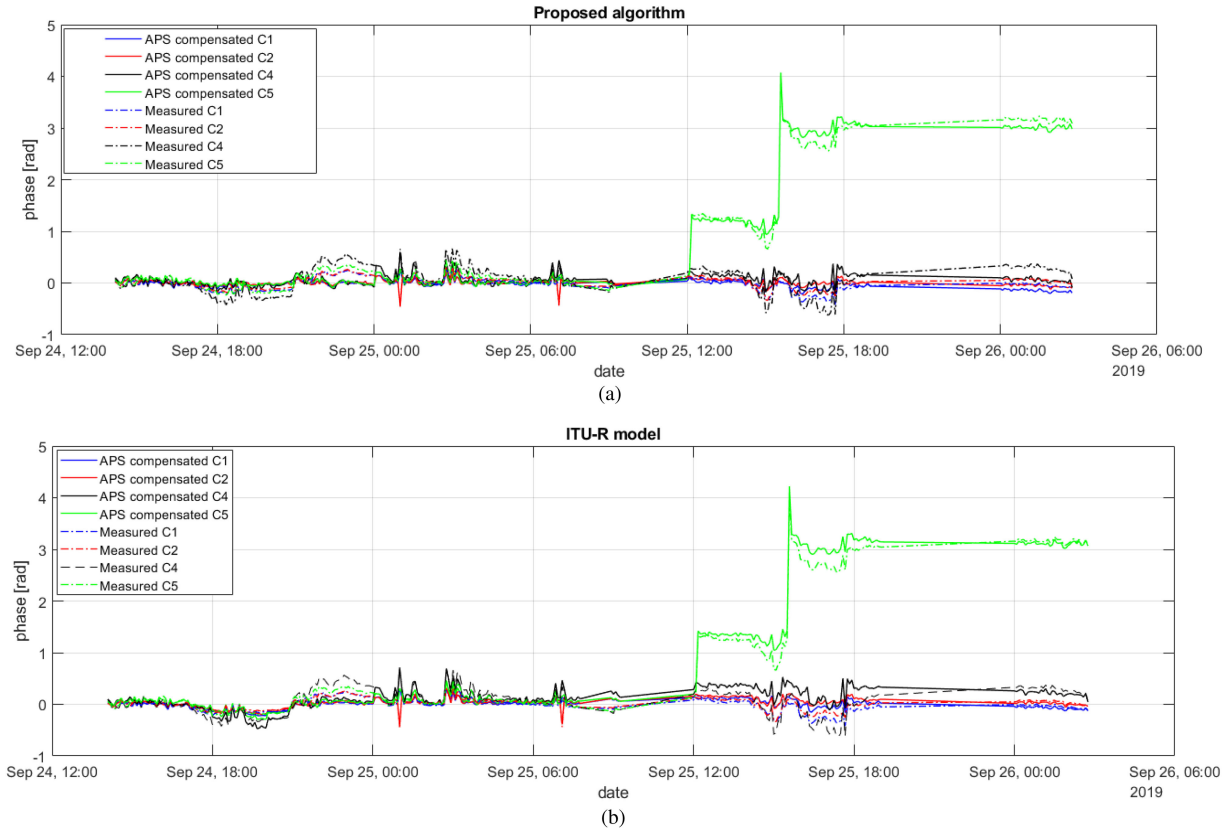
Fig. 10.   Interferometric phase after atmospheric effect compensation. The top image refers to the application of the proposed approach, while the bottom image refers to the application of the ITU-R model. In each image, the colored dashed lines represent the measured interferometric phase. Each color refers to a corner reflector. The colored solid lines represent the interferometric phase after APS compensation. This image refers to data acquired from 24 September 2019 14:05 to 26 August 2019 02:45.

TABLE V
LEAVE-ONE-OUT ANALYSES OF THE PROPOSED APPROACH

	Leave-C2	Leave-C1	Leave-C4
$\mu[rad]$	2.8987	2.88095	3.00338
$\sigma[rad]$	0.11249	0.11713	0.10939
$\mu[mm]$	5.08833	5.05718	5.2720
$\sigma[mm]$	0.2150	0.20561	0.19203
$\Delta\phi_{min}[rad]$	2.76305	2.74737	2.86834
$\Delta\phi_{max}[rad]$	3.4749	3.115524	3.21979
$\Delta\phi_{min}[mm]$	4.48502	4.8227	5.035
$\Delta\phi_{max}[mm]$	5.5525	5.4899	5.652

Each column reports the statistical values of the estimates, obtained by leaving out one of the corner reflector and using the proposed approach. As for example, the "Leave-$C2$" experiment means that only $C1$ and $C4$ scatterers have been used to estimate α and β. Values refer to the first time interval, when the scatterer is moved of 5 mm.

TABLE VI
LEAVE-ONE-OUT ANALYSES OF THE PROPOSED APPROACH

	Leave-C2	Leave-C1	Leave-C4
μ_{rad}	1.2287	1.1988	1.2715
σ_{rad}	0.02428	0.02456	0.02221
μ_{mm}	2.1569	2.1044	2.23202
σ_{mm}	0.0426	0.0431	0.0390
$\Delta\phi_{min_{rad}}$	1.1832	1.152	1.231
$\Delta\phi_{max_{rad}}$	1.286	1.2561	1.3191
$\Delta\phi_{min_{mm}}$	2.077	2.024	2.162
$\Delta\phi_{max_{mm}}$	2.257	2.205	2.315

Each column reports the statistical values of the estimates, obtained by leaving-out-one of the corner reflector. Values refer to the first time interval, when the scatterer is moved of 2 mm.

VI. DISCUSSIONS AND REMARKS

The proposed approach has been conceived by considering pros and cons of both model-based and data-driven approaches for APS in GB-SAR applications and by taking into account our purposes, namely, the detection of tiny subsidence of the terrain of the order of a millimeter of even smaller. Model-based algorithms make use of a refractive index's model and measurements of the weather parameters. Conversely, data-driven algorithms make use of the measured interferometric phase of persistent scatterers or GCPs to estimate the changes in the refractive index, without using any measurements of the weather parameters. Typically, GCPs are extracted based on their coherence. However, very tiny subsidence in the terrain do not affect much the coherence, which remains quite high, hence making the identification of "true" GCPs problematic. Nonstationary GCPs may, therefore, affect the estimate process in the data-driven-based
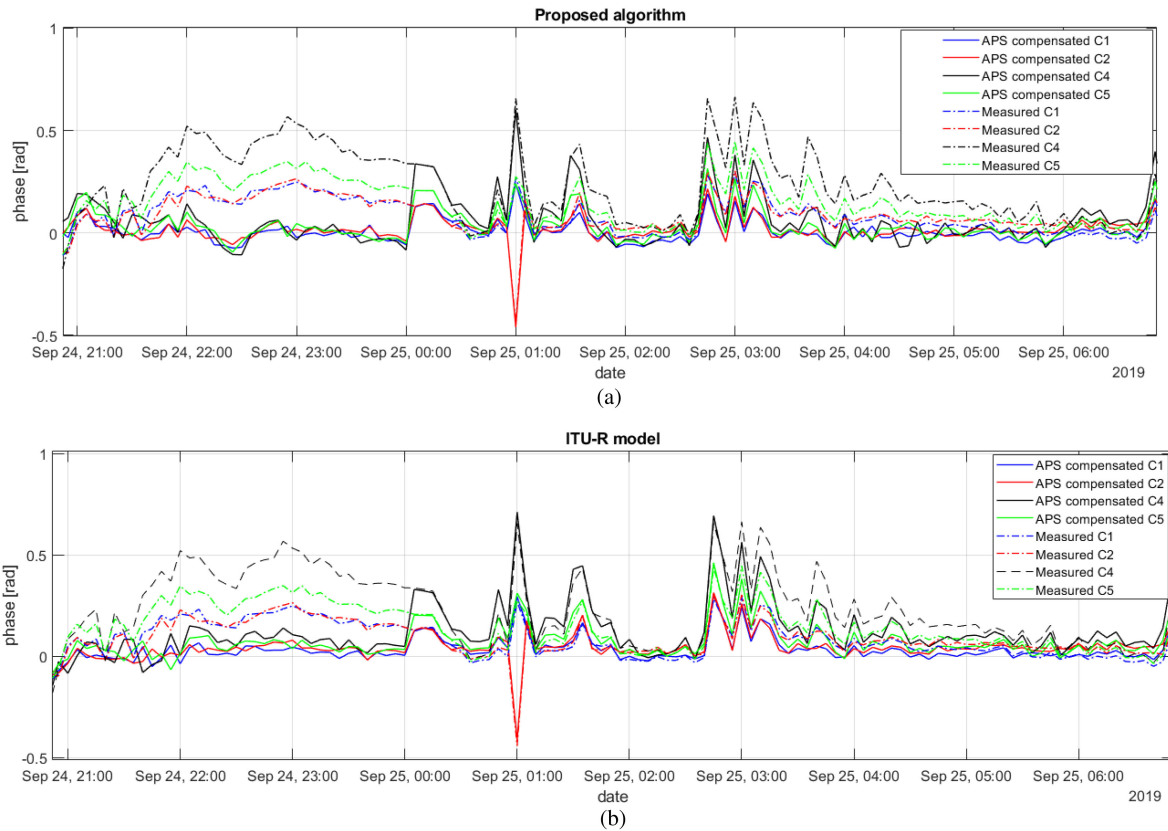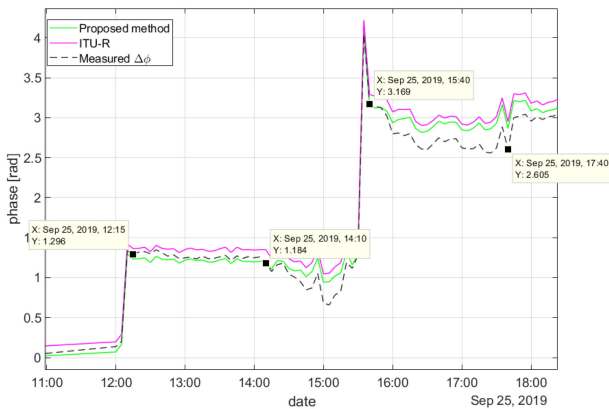
Fig. 11. (a) and (b) Magnification of Fig. 10.

Fig. 12. Comparison between the measured and residual interferometric phases of the nonstationary scatterer. The dark, green, and pink lines are, respectively, the measured interferometric phase, the interferometric phase after the application of the proposed approach, and the residual interferometric phase after the application of the ITU-R model.

the wet and dry components that compose the refractive index's model as defined in the ITU-R standards. The estimation process is conducted using a least squares approach and the measured interferometric phases of the GCPs. The proposed approach relies on the spatial homogeneity assumption of the refractive index, which typically holds for relatively small areas of roughly few kilometers. To address this issue, the weights of the proposed model are averaged over spatially distributed scatterers. As can be noted by observing Fig. 5, the estimated weights at each GCP have the same trend but slightly different values. Their average, therefore, can handle the spatial variability and noise. However, if large areas are observed, the proposed approach can be applied in a piecewise way. This operative mode may additionally handle changes in the elevation of the terrain. Another way to relax the homogeneity assumption would be to modify the refractive index's model by including dependence of the refractive index on the terrain elevation. This will be part of our future studies on APS removal for submillimeter subsidence detections and estimation.

VII. CONCLUSION

The proposed approach can be considered as a middle algorithm in between what we have defined model-based and data-driven approaches. Since it aimed to optimize the refractive index model defined in the ITU-R standard, it was compared with the ITU-R model as defined in [18] and (6). The comparative analysis showed that the proposed algorithm always

algorithms. Conversely, the use of refractive index's models, describing the way the troposphere changes the speed of the wave in the medium, avoids the selection of GCPs. However, we found that the refractive index's model defined in [18] and (6) might not always match well with the measured refractive index. Hence, we have proposed an algorithm that relies on physics of the refractive index but uses some GCPs to better fit the model to the acquired data. GCPs are used to estimate the weights of

performs better than the one based on the use of the ITU-R model. Specifically, the proposed algorithm provided a lower residual phase mean error, around 0.02 mm, and a lower standard deviation of the residual phase, 0.06 mm. A further test was also conducted in case of a true terrain movement. A data frame was considered, where a corner reflector placed on a micrometric tripod was shifted by 2 and 5 mm on September 25 at 12:00 and at 15:30, respectively. The results showed that the proposed approach contributes to significantly reducing the standard deviation of the residual interferometric phase and providing an improved estimate of the true displacement, if compared with the ITU-R-based algorithm.

REFERENCES

[1] L. Noferini *et al.*, "Permanent scatterers analysis for atmospheric correction in ground-based SAR interferometry," *IEEE Trans. Geosci. Remote Sens.*, vol. 43, no. 7, pp. 1459–1471, Jul. 2005.

[2] Y. Izumi, L. Zou, K. Kikuta, and M. Sato, "Iterative atmospheric phase screen compensation for near-real-time ground-based InSAR measurements over a mountainous slope," *IEEE Trans. Geosci. Remote Sens.*, vol. 58, no. 8, pp. 5955–5968, Aug. 2020.

[3] L. Pipia, X. Fabregas, A. Aguasca, and C. Lopez-Martinez, "Atmospheric artifact compensation in ground-based DInSAR applications," *IEEE Geosci. Remote Sens. Lett.*, vol. 5, no. 1, pp. 88–92, Jan. 2008.

[4] L. Iannini and A. M. Guarnieri, "Atmospheric phase screen in ground-based radar: Statistics and compensation," *IEEE Geosci. Remote Sens. Lett.*, vol. 8, no. 3, pp. 537–541, May 2011.

[5] R. F. Hanssen, *Radar Interferometry: Data Interpretation and Error Analysis* (Remote Sensing and Digital Image Processing Series). Dordrecht, The Netherlands: Springer, 2001.

[6] H. J. Liebe, "Modeling attenuation and phase of radio waves in air at frequencies below 1000 GHz," *Radio Sci.*, vol. 16, no. 6, pp. 1183–1199, 1981.

[7] A. Barucci *et al.*, "Universal fluctuations in tropospheric radar measurements," *Europhys. Lett.*, vol. 89, no. 2, 2010, Art. no. 20006.

[8] X. Cong and M. Eineder, "Volcano deformation measurement using persistent scatterer interferometry with atmospheric delay corrections," in *Proc. 9th Eur. Conf. Synthetic Aperture Radar*, 2012, pp. 681–684.

[9] H. A. Zebker, P. A. Rosen, and S. Hensley, "Atmospheric effects in interferometric synthetic aperture radar surface deformation and topographic maps," *J. Res. Nat. Bur. Standards*, vol. 102, no. B4, pp. 7547–7563, 1997.

[10] G. Fornaro, N. D'Agostino, R. Giuliani, C. Noviello, D. Reale, and S. Verde, "Assimilation of GPS-derived atmospheric propagation delay in DInSAR data processing," *IEEE J. Sel. Topics Appl. Earth Observ. Remote Sens.*, vol. 8, no. 2, pp. 784–799, Feb. 2015.

[11] S. Baffelli, O. Frey, and I. Hajnsek, "Geostatistical analysis and mitigation of the atmospheric phase screens in Ku-band terrestrial radar interferometric observations of an Alpine glacier," *IEEE Trans. Geosci. Remote Sens.*, vol. 58, no. 11, pp. 7533–7556, Nov. 2020.

[12] D. Leva, G. Nico, D. Tarchi, J. Fortuny-Guasch, and A. Sieber, "Temporal analysis of a landslide by means of a ground-based SAR interferometer," *IEEE Trans. Geosci. Remote Sens.*, vol. 41, no. 4, pp. 745–752, Apr. 2003.

[13] G. Luzi *et al.*, "Ground-based radar interferometry for landslides monitoring: Atmospheric and instrumental decorrelation sources on experimental data," *IEEE Trans. Geosci. Remote Sens.*, vol. 42, no. 11, pp. 2454–2466, Nov. 2004.

[14] N. Dematteis, G. Luzi, D. Giordan, F. Zucca, and P. Allasia, "Monitoring Alpine glacier surface deformations with GB-SAR," *Remote Sens. Lett.*, vol. 8, no. 10, pp. 947–956, 2017.

[15] R. Iglesias *et al.*, "Atmospheric phase screen compensation in ground-based SAR with a multiple-regression model over mountainous regions," *IEEE Trans. Geosci. Remote Sens.*, vol. 52, no. 5, pp. 2436–2449, May 2014.

[16] A. Karunathilake and M. Sato, "Atmospheric phase compensation in extreme weather conditions for ground-based SAR," *IEEE J. Sel. Topics Appl. Earth Observ. Remote Sens.*, vol. 13, pp. 3806–3815, 2020.

[17] M. Shi *et al.*, "An improved method for InSAR atmospheric phase correction in mountainous areas," *IEEE J. Sel. Topics Appl. Earth Observ. Remote Sens.*, vol. 14, pp. 10509–10519, 2021.

[18] *The Radio Refractive Index: Its Formula and Refractivity Data*, Recommendation ITU-R P.453-11, 2015.

Elisa Giusti (Member, IEEE) received the Laurea degree in telecommunication engineering (*cum laude*) and Ph.D. degrees in remote sensing from the University of Pisa, Pisa, Italy, in 2006 and 2010, respectively.

From June 2009 to November 2014, she was a Researcher under contract with the Department of Information Engineering, University of Pisa. From November 2014 to December 2015, she was a Research under contract with the National Laboratory of Radar and Surveillance Systems, National Inter-University Consortium for Telecommunications, Pisa, where she has been a permanent Researcher since December 2015. Since 2009, she has been involved as a Researcher in several international projects funded by Italian ministries (Ministry of Defence and Ministry of Economic Development) and European organizations (European Defence Agency and European Space Agency). She is a Co-Founder of a radar-systems-related spin-off company, "ECHOES radar technologies," Pisa. She is a co-author of more than 60 papers and three book chapters. She is an Editor of a book entitled *Radar Imaging for Maritime Observation* (Boca Raton, FL, USA: CRC Press, 2018). Her research interests are mainly in the field of radar imaging, including active, passive, bistatic, multistatic, and polarimetric radar.

Dr. Giusti was the recipient of the 2016 Outstanding Information Research Foundation Book Publication Award for the book entitled *Radar Imaging for Maritime Observation*.

Samuele Gelli received the Laurea degree in telecommunication engineering and Ph.D. degree in remote sensing from the University of Pisa, Pisa, Italy, in 2013 and 2017, respectively.

From 2017 to 2019, he was a Postdoctoral Researcher with the Department of Information Engineering, University of Pisa. He is currently a permanent Researcher with the National Laboratory of Radar and Surveillance Systems, National Inter-University Consortium for Telecommunications, Pisa. His research interests are mainly in the field of radar imaging and radar signal processing, including synthetic aperture radar (SAR) and inverse SAR imaging, cognitive radar systems, interference suppression, and target detection.

Marco Martorella (Fellow, IEEE) received the Laurea degree (bachelor's and master's) (*cum laude*) in telecommunication engineering and the Ph.D. in remote sensing from the University of Pisa, Pisa, Italy, in 1999 and 2003, respectively.

He is currently an Associate Professor with the Department of Information Engineering, University of Pisa. He is an external Professor with the University of Cape Town, Cape Town, South Africa, where he lectures within the master's in radar and electronic defense. He is also the Director of the National Laboratory of Radar and Surveillance Systems, National Inter-University Consortium for Telecommunications, Pisa. He is the author of more than 250 international journal and conference papers, three books, and 17 book chapters. He has presented several tutorials at international radar conferences, has lectured at NATO Lecture Series, and has organized international journal special issues on radar imaging topics. He is a Co-Founder of ECHOES, a radar-systems-related spin-off company. His research interests are mainly in the field of radar, with a specific focus on radar imaging, multichannel radar, and space situational awareness.

Prof. Martorella is a member of the IEEE Aerospace and Electronic Systems Society Radar Systems Panel, a member of the NATO Sensors and Electronics Technology (SET) Panel, where he sits as the Chair of the Radio Frequency Technology Focus Group, and a member of the European Defence Agency Radar CapTech. He has chaired several NATO research activities, including three Research Task Groups, one Exploratory Team, and two Specialist Meetings. He was recipient of the 2008 Italy–Australia Award for Young Researchers, the 2010 Best Reviewer for IEEE GEOSCIENCE AND REMOTE SENSING LETTERS, the IEEE 2013 Fred Nathanson Memorial Radar Award, the 2016 Outstanding Information Research Foundation Book Publication Award for the book entitled *Radar Imaging for Maritime Observation*, and the 2017 NATO SET Panel Excellence Award.